Characterization of Viscoelastic Media Combining Ultrasound and Magnetic-Force Induced Vibrations on an Embedded Soft Magnetic Sphere

Alejandro Cebrecos, Noé Jiménez, *Member, IEEE*, Rafael Tarazona, Miguel Company, José María Benlloch, and Francisco Camarena

***Abstract*— We report a method to locally assess the complex shear modulus of a viscoelastic medium. The proposed approach is based on the application of a magnetic force to a millimeter-sized steel sphere embedded in the medium and the subsequent monitoring of its dynamical response. A coil is used to create a magnetic field inducing the displacement of the sphere located inside a gelatin phantom. Then, a phased-array system using 3 MHz ultrasound probe operating in pulse-echo mode is used to track the displacement of the sphere. Experiments were conducted on several samples and repeated as a function of phantom temperature. The dynamic response of the sphere measured experimentally is in good agreement with Kelvin–Voigt theory. Since the magnetic force is not affected by weak diamagnetic media, our proposal results in an accurate estimation of the force acting on the inclusion. Consequently, the estimated viscoelastic parameters show excellent robustness and the elastic modulus agrees with the measurements using a quasi-static indentation method, obtaining errors below 10% in the whole temperature range. The use of the macroscopic inclusion limits the direct application of this method in a biomedical context, but it provides a robust estimation of the elastic modulus that can be used for material characterization in industrial applications.**

***Index Terms*— Magnetic force, magneto-motive, shear modulus, ultrasound, viscoelasticity.**

I. Introduction

THE assessment of the mechanical properties of viscoelastic media is of great interest in medicine, where biomechanical properties of tissue have been proved to be often correlated with their physiological state [1]–[3], and in industry, where the knowledge of the mechanical properties of the medium allow to predict the properties, appearance, processing, and performance of polymers [4], [5], concrete [6], [7], asphalt [8], or food [9], [10].

The mechanical response of a solid sphere subjected to the effect of an external force can be used to determine the viscoelastic properties of the surrounding medium. This relation was first explored theoretically by Oestreicher considering a Kelvin–Voigt rheological model in a medium with equal stiffness and viscosity [11]. Later, Ilinskii *et al.* [12] obtained the static and transient displacement responses of a sphere and a bubble embedded in an elastic medium, and Aglyamov *et al.* [13] extended the work to viscoelastic media. Finally, Urban *et al.* [14] proposed a theoretical development to describe the generalized embedded sphere response both in time and frequency domains so that any viscoelastic rheological model can be used.

From these theoretical works, several studies have been carried out to locally characterize tissue-like phantoms by exciting a sphere using the acoustic radiation force (ARF) produced at the focus of an ultrasonic beam. The group of Prof. Greenleaf presented a quantitative model for a sphere vibrated by two ultrasound beams of nearby frequencies able to estimate the material properties of the medium surrounding a sphere [15]. Later, the group of Prof. Emelianov locally assessed the shear modulus of a medium by using the ARF generated at the focus of a focused ultrasound beam excited with a short pulse [16]. In addition, the motion of the media due to magnetomotive-generated shear waves can also be measured [17], but to our knowledge, this method has not been applied to estimate the viscoelastic parameters of the medium.

In this article, we propose a new method to estimate the viscoelastic parameters of soft-solids. We use a classical magneto-motive ultrasound (MMUS) experimental setup [18]–[22] to track the dynamics of a macroscopic steel sphere embedded in a gelatin phantom excited by an external magnetic force, as sketched in Fig. 1. First, a coil is excited with an electrical pulse. Second, the generated magnetic field produces a transient attracting force on the soft magnetic inclusion. Third, using a 64-channel

Manuscript received March 30, 2021; accepted July 14, 2021. Date of publication July 16, 2021; date of current version November 23, 2021. This work was supported in part by the Spanish Ministry of Science, Innovation and Universities through the "Juan de la Cierva - Incorporación" under Grant IJC2018-037897-I, in part by the Program "Proyectos I+D+i 2019" under Grant PID2019-111436RB-C22, in part by the Agència Valenciana de la Innovació under Grant INNCON/2021/8, in part by Generalitat Valenciana under Grant AICO/2020/268, and in part by the European Union through the Programa Operativo del Fondo Europeo de Desarrollo Regional (FEDER) of the Comunitat Valenciana 2014–2020 under Grant IDIFEDER/2018/022. The work of Alejandro Cebrecos was supported by the Universitat Politècnica de València under Program PAID-10-19. *(Corresponding author: Noé Jiménez.)*

The authors are with the Instituto de Instrumentación para Imagen Molecular, Universitat Politècnica de València, Consejo Superior de Investigaciones Científicas, 46022 Valencia, Spain (e-mail: nojigon@upv.es).

Digital Object Identifier 10.1109/TUFFC.2021.3097883

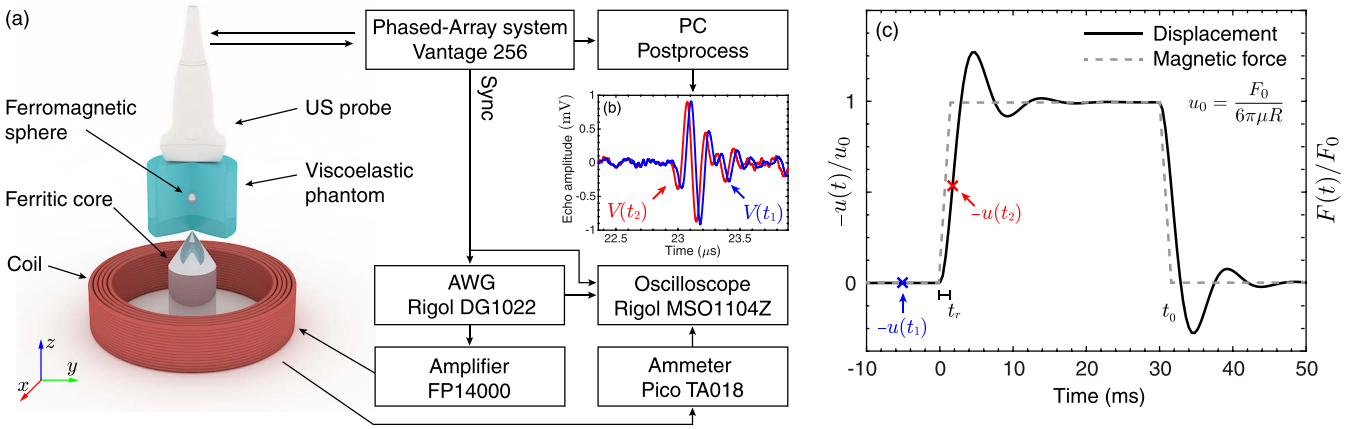

Fig. 1. (a) Sketch and block diagram of the experimental setup. (b) Example of ultrasonic pulse-echo signals: blue line ($V_{\triangleright}t_1{}_{\triangleleft}$) corresponds to the echo of the sphere at reference position in absence of magnetic force, while red line [$V(t_2)$] corresponds to the echo signal an instant when the magnetic force is present, as indicated in (c) by the color markers. (c) Magnetic force waveform (dashed line) corresponding to a trapezoidal pulsed excitation of length t_0 with a rise time of t_r, and expected displacement waveform (continuous line) as a result of the cross correlation between multiple ultrasonic pulse-echo signals at each time.

phased-array system, the position of the inclusion is dynamically tracked, and by using cross correlation methods the time-varying displacement waveform of the sphere is obtained. Finally, the elastic parameters of the surrounding viscoelastic medium are estimated from the dynamics of the sphere.

The procedure is similar to the one used in previous works that make use of ARF [15], [16], but, in this case, we use a magnetic force acting on a soft magnetic inclusion. A common problem in ARF-based techniques is that it is difficult to accurately measure or estimate the magnitude of the applied force. This is mainly caused because ultrasound waves attenuate as they propagate into heterogeneous tissues, the magnitude of the ARF depends on the geometry and properties of the object itself and tissue absorption, and in addition weakly nonlinear effects can be relevant to the estimation of the ARF. The uncertainty in the estimation of the ARF directly has an impact on the accuracy of the estimated viscoelastic parameters. In contrast, since the magnetic force is almost not affected by tissues which are, in general, weak diamagnetic media, our proposal results in an accurate estimation of the force acting on the sphere. In addition, ARF should induce motion not only at the bead but on the viscoelastic media due to ultrasound attenuation and scattering at heterogeneities. Using a magnetic force, only the sphere is pulled. Therefore, it increases the robustness of the estimation of the viscoelastic parameters of the surrounding medium.

It is important to remark that while the setup is similar to MMUS techniques that track the motion of a soft-solid produced by magnetic nanoparticles [18]–[22], we make use of a millimeter-size steel sphere. As we will demonstrate, the use of this inclusion allows an accurate estimation of the force exerted on it, enabling the quantitative estimation of the viscoelastic parameters.

The article is structured as follows: Section II presents the theoretical model to describe the dynamics of a solid sphere embedded in a viscoelastic medium and to evaluate the magnetic force on the sphere. Section III shows the experimental setup and methods. Section IV provides the experimental results and their comparison using indentation techniques. Finally, the concluding remarks are given in Section V.

II. Model

A. Dynamics of a Solid Sphere Embedded in Viscoelastic Media

The bulk modulus of most soft-tissues and tissue phantoms is several orders of magnitude higher than their shear moduli. Therefore, to model low-frequency shear deformations these media can be considered an incompressible viscoelastic medium, whose equations of motion for a Kelvin–Voigt-type medium are given by Aglyamov *et al.* [13]

$$\rho\frac{\partial^2\mathbf{u}}{\partial t^2} = -\nabla p + \mu\nabla^2\mathbf{u} + \eta\nabla^2\frac{\partial\mathbf{u}}{\partial t} \tag{1}$$

where $\mathbf{u} = \mathbf{u}(t,\mathbf{r})$ is the displacement vector, $p = p(\mathbf{r})$ is the internal pressure, μ and η are the shear elastic and shear viscous coefficients, ρ is the density of the medium and t is the time. Assuming a Fourier convention of $e^{-i\omega t}$, the equations of motion in the frequency domain are written as

$$-\nabla P + G\nabla^2\mathbf{U} + \rho\omega^2\mathbf{U} = 0 \tag{2}$$

where P and $\mathbf{U}$ are the Fourier transforms of p and $\mathbf{u}$, ω is the angular frequency and $G = (\mu - i\omega\eta)$ is the complex shear modulus. We consider a rigid sphere embedded in an infinite and homogeneous viscoelastic medium submitted to a transient external force $F_z^{\text{ext}}(t)$, acting on direction z. In the frequency domain, and for small displacements, the z component of the displacement of the sphere $U_z(\omega)$ and the Fourier transform of the external force $F_z^{\text{ext}}(\omega)$ are linearly related by Ilinskii *et al.* [12]

$$F_z^{\text{ext}}(\omega) = \left[-M\omega^2 + 6\pi GR\left(1 - ikR - \frac{1}{9}k^2R^2\right)\right]U_z(\omega) \tag{3}$$

where $M = 4\pi\rho_s R^3/3$ is the mass, ρ_s the density, R is the radius of the solid sphere, and k is the complex wavenumber in the viscoelastic medium given by the dispersion relation $k^2 = \rho\omega^2/(\mu - i\omega\eta)$. Then, the displacement of the

sphere $u_z(t)$ in time domain can be recovered using the inverse Fourier transform as

$$u_z(t) = \frac{1}{2\pi}\int_{-\infty}^{\infty} U_z(\omega)\mathrm{e}^{-i\omega t}d\omega. \tag{4}$$

In our study, we submit the sphere to a pulsed magnetic force. In practice, obtaining an ideal rectangular waveform for the current is not possible due to the inductance of the coil. Therefore, we assume that the temporal evolution of the magnetic force is given by a trapezoidal pulse with a finite rise time, as shown in Fig. 1(c), as

$$F_z^{\mathrm{trap}}(t) = \begin{cases} -F_0\left(\dfrac{t}{t_r}\right) & 0 \le t \le t_r \\ -F_0 & t_r \le t \le t_0 \\ -F_0\left(1 - \dfrac{t-t_0}{t_r}\right) & t_0 \le t \le t_0 + t_r \\ 0 & t > t_0 + t_r \end{cases} \tag{5}$$

where t_0 is the pulse duration, F_0 is the amplitude of the pulse, and t_r is the rise time. The Fourier transform of the trapezoidal pulsed force results in

$$F_z^{\mathrm{trap}}(\omega) = -\frac{F_0}{t_r\omega^2}\left(e^{i\omega t_0} - 1\right)\left(e^{i\omega t_r} - 1\right). \tag{6}$$

Combining (3) and (6) and applying the inverse Fourier transform (4), the displacement of the solid sphere in a viscoelastic medium is written in the time domain as

$$u_z^{\mathrm{trap}}(t) = -\frac{F_0}{12\pi^2 R t_r}\int_{-\infty}^{\infty} \times \frac{\left(\mathrm{e}^{i\omega t_0} - 1\right)\left(\mathrm{e}^{i\omega t_r} - 1\right)\mathrm{e}^{-i\omega t}}{\omega^2(\mu - i\omega\eta)\left(1 - ikR - k^2R^2(1+2\beta)/9\right)}d\omega \tag{7}$$

where $\beta = \rho_s/\rho$ is the normalized density of the sphere with respect to the medium density, in analogy with the expression obtained in [12] for a rectangular pulsed excitation. Equation (7) is integrated numerically to obtain the theoretical estimation of the displacement of the sphere. Note the displacement of the sphere for a long pulse converge to a constant value [12] of $u_0 = F_0/6\pi\mu R$, as is shown in the example in normalized scale in Fig. 1(c).

B. Magnetic Force Exerted on the Sphere

The magnetic force acting on a small ellipsoid of volume V due to the presence of the magnetic flux density B_0 along the z-axis is given by Schenck [23]

$$F_z^{\mathrm{ext}}(z,t) = \frac{\chi V}{\mu_0}B_0(z,t)\frac{\partial B_0(z,t)}{\partial z}\left[\frac{\cos^2\theta}{1+\chi D_a} + \frac{\sin^2\theta}{1+\chi D_r}\right] \tag{8}$$

where χ is the volumetric magnetic susceptibility of the particle (neglecting the magnetic susceptibility of the background), μ_0 is the magnetic permeability in vacuum, D_a is the demagnetizing factor along the axis of symmetry, D_r is the radial demagnetizing factor, and θ is the angle between the symmetry axis of the particle (x-direction) and the magnetic field direction (z-axis). For a spherical particle, $D_a = D_r = 1/3$, other relations can be found for other geometries [23].

The soft magnetic sphere used in this experiment is made of a low-alloy chrome steel (AISI 52100), having a relative magnetic permeability $\mu_r > 300$, therefore, the volumetric magnetic susceptibility $\chi \gg 1$, thus, it can be considered as a soft magnetic material [24]. As such, and considering that all experiments in this study are performed at relatively low values of magnetic field (around 100 mT), insufficient to saturate the material, both coercivity and hysteresis are relatively small and are neglected for this material in our experiments [25]. Note the magnetic saturation of the sphere can be roughly estimated as around 2 T for a low-alloy steel with less than 2% of chromium [26]. Therefore, and taking into consideration, the spherical geometry of the bead aligned with the magnetic field, at the z-axis of the axisymmetric system, the force acting in the soft magnetic sphere of radius R can be reduced to [23]

$$F_z^{\mathrm{ext}}(z,t) = -\frac{4\pi R^3}{\mu_0}B_z(z,t)\frac{\partial B_z(z,t)}{\partial z}. \tag{9}$$

Note that for a soft magnetic sphere the ratio between the magnetic field strength, $\mathbf{H}$, and the magnetization of the material, $\mathbf{M}$, does not depend on the magnetic properties of the material [27] and is given by $\mathbf{H} = -3\mathbf{M}$, the induced mechanical force is, therefore, independent of χ. Also note that (9) can only be applied if the system is axisymmetric, i.e., the sphere must be accurately located at the axis of the ferritic core. To know the magnetic force amplitude as a function of the electrical current on the coil, a finite element method (FEM) simulation of the whole magnetic system was carried on using COMSOL 5.2 software. Numerical simulations were carried out and the magnetic field was calculated at different distances from the center of the ferritic core for different values of electrical current. A phenomenological model was obtained by fitting the simulated data to the power-law

$$F_0(z, I_0) = I_0^2\alpha z^{\gamma}, \tag{10}$$

where I_0 is the electrical current on the coil, z is the distance from the ferritic core to the sphere, and α and γ are the fitted parameters of the model. This model, as we will show below, was validated using (9) and experimental measurements of the magnetic field, and direct measurements of the force on a soft magnetic sphere using a magnetic scale. The model provides a direct estimation of the force acting on the sphere as a function of the electrical current in the coil and the position of the sphere, parameters that can be accurately measured.

III. Experimental Methods

The experimental setup that produces the magnetic force on the soft magnetic sphere is shown in Fig. 1(a). On the one hand, we use a copper coil (S1013, Solen Inc., Saint-Hubert, QC, Canada) with a height of 45 mm and a radius of 178 mm. Inside the coil is located a ferritic steel core (AISI 430 steel) with a radius of 35 mm. The coil is excited with a 2800 W power amplifier (FP14000) which receives the excitation signal from an arbitrary waveform generator (Rigol DG1022). In particular, we excite the coil with the proper waveforms to create trapezoidal pulses of electrical current in the coil of $t_0 = 30$ ms duration. An ammeter (TA018, Pico Technology) is used to observe the current in

the coil and evaluate the quality of the trapezoidal pulse. We measured a rising time of $t_r = 3$ ms. A three-axis Hall magnetometer (THM1176, Metrolab) is used to characterize the magnetic field of the system at a steady current. The field sensitive volume of the probe is 200 μm $\times$ 200 μm $\times$ 5 μm, the instrument range is up to 3 T with a resolution 0.1 mT, and it provides an accuracy of $\pm 1\%$ T. Finally, a weighing scale (Cent-O-Gram Model 311, OHAUS, Moscow, Russia) is used to experimentally measure the magnetic force exerted on the soft magnetic sphere (AISI 52100 steel) at different heights in the absence of the viscoelastic medium and under a current of $I_0 = 30$ A. In this regard, the original pan of the balance was removed and substituted by few pieces of lead having the same weight as the original pan. Then, a nylon thread was attached to the balance on one side and to the metallic sphere on the other, making sure that every metallic part of the balance scale was placed at a distance far enough to avoid any detectable influence of the pulling force. This allows us to validate the force model given by (9). Note that the magnetic force acting on the sphere depends on the distance to the ferritic core. However, the displacements considered here are smaller than 100 μm and the force presents spatial variations that are below 1%. Therefore, we assume that the magnetic force does not depend on the sphere displacement, only on its position at rest.

The displacement of the sphere is estimated from the temporal shifts of the echoes produced by a phased-array system (Vantage 256, Verasonics, Kirkland, WA, USA) using a 64-channel 3 MHz ultrasound probe (P4-2V, Verasonics, Kirkland, WA, USA) as shown in Fig. 1(b) and (c). The phased-array is set to a pulse repetition frequency of 4 kHz, allowing the reception of an echo every 0.25 ms. The radio frequency (RF) signals from the ultrasound probe are acquired by the phased-array with a total recording duration of 75 ms. The position of the sphere is given by the cross correlation between the RF signals and a reference signal in which the sphere is at rest, i.e., in its initial state without being magnetically excited [28]. Interpolation up to a sampling frequency of 15.6 GHz is considered here to increase the accuracy on the estimated displacements up to a resolution of 0.1 μm.

We consider two different gelatin phantoms of cylindrical shape with a diameter of 30 mm and a volume of 25 ml. First, "phantom A" was produced mixing water and 200 Bloom gelatin powder, with a gelatin concentration of 60 g/l. Second, "phantom B" was produced by mixing water, glycerol (99.5% purity), and 200 Bloom gelatin powder, with a concentration of 60 g/L and a glycerol concentration of 40% of the total volume. The density of both phantoms was measured independently, obtaining slightly different densities for both phantoms, as expected ($\rho_A = 1010$ kg/m^3, $\rho_B = 1080$ kg/m^3). A 2.000 $\pm$ 0.001 mm diameter soft magnetic sphere of normalized steel (AISI 52100) was introduced during the manufacturing of both phantoms at about 15 mm from the bottom surface. The sphere was attached to a nylon thread fastened to a vertical axis and introduced inside the phantoms while they were still liquid, easing a precise positioning of the sphere. The location of the sphere was measured using pulse-echo measurements.

The measurement procedure is as follows: first, the sample is prepared and located in front of the ferritic core as shown in Fig. 1(a). Second, the coil is electrically excited and a pulsed magnetic force is generated on the soft magnetic sphere. Third, the motion of the sphere is tracked by the phased-array system. Finally, the viscoelastic parameters of the medium are obtained by minimization techniques. We use a curve-fitting algorithm to optimize the values of μ and η that minimizes the least-squares error between the experimental displacement waveform and the theoretical one given by (7). Note that the value of the magnetic force is fixed during the minimization process. This procedure is repeated three times in this work for each experiment.

Experiments were carried out at an increasing temperature, taking the samples from a refrigerator and letting them slowly achieve room temperature. Measurements were taken ranging from 16° to 26 °C. The temperature was measured using two thermistor probes (Tinytag Temperature Logger TK 4023). The first thermistor was located inside the phantom at the same height of the sphere on the lateral wall of the sample container while the second probe was placed on the top surface of the phantom.

Finally, indentation tests were performed using a mechanical testing machine calibrated to measure the bloom strength of gelatins (TAXTExpress, Texture Technologies Corporation, Hamilton, MA, USA). We used a flat-ended cylinder indenter of radius $a = 1/4$ in, compressing the samples at a rate of 0.5 mm/s. A maximum displacement of 1 mm was set. The shear modulus was calculated by fitting the force, $F(\Delta z)$, to $F(\Delta z) = 8\, a \mu \Delta z$ where Δz is the indentation depth [29], [30]. Indentation tests were repeated at different temperatures ranging from 20° to 26 °C.

IV. Results

A. Magnetic Field and Force Characterization

We start showing the calibration and validation of the magnetic forces acting on the sphere in the absence of viscoelastic medium. First, the simulated magnetic field in the absence of sphere is shown in Fig. 2(a). As expected, the magnetic field is highly enhanced near the tip of the ferritic core. Second, a direct measurement of the magnetic field of the system in the static regime has been carried out around the area in which the steel sphere will be located, feeding the coil using in this case a continuous current of 20 A. The value of the z component of the magnetic field was sampled along three horizontal sweeps of 40 mm in length with a 1 mm pitch in x-direction, at 10, 15, and 20 mm height from the core, as shown in Fig. 2(b). The experimental data is in excellent agreement with the simulated magnetic flux density. Simulations including the sphere show that the small soft magnetic bead do not remarkably disturb the field outside the boundaries of the sphere [see dashed gray lines in Fig. 2(b)]. Finally, the magnetic force as a function of the distance to the coil, i.e., at the axis of symmetry, is shown in Fig. 2(c). First, the magnetic force was estimated using the simulated magnetic field and (9) as a function of the height. This was repeated for different currents (from 5 to 50 A), and (10) was fitted in a least-squares sense to the simulated force distribution in the range 5 mm $< z <$ 25 mm, obtaining

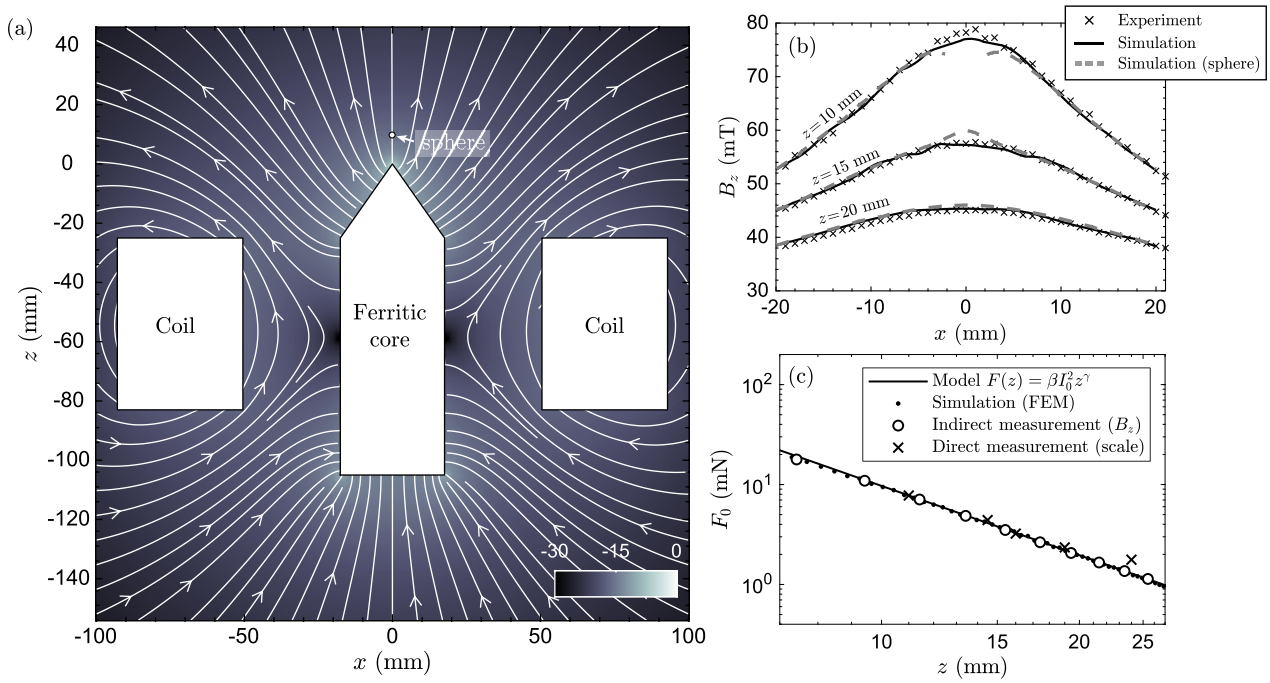

Fig. 2. (a) Scheme of the coil and ferritic core, FEM simulated magnetic flux density, and field lines (white). Colormap in $10\log_{10}|B|/|B|_{\max}$ units. (b) Experimental (markers), simulated (continuous) and simulated including the sphere (dashed-gray) magnetic flux density at heights $z = 10$ mm, $z = 15$ mm and $z = 20$ mm. (c) Magnetic force exerted on the sphere measured experimentally using weighing scale (crosses), calculated from the measured magnetic field (circles), simulated using FEM (dots) and model retrieved using simulated data (continuous line).

the parameters $\alpha = 2.66 \cdot 10^{-10}$ N/A^2 m$^\gamma$ and $\gamma = -2.3$. To validate this model, the magnetic field was experimentally measured along the axial direction from the tip of the core, from 3 to 24 mm, and using (9) the magnetic force was calculated. In addition, the force was directly measured using a weighing scale with an accuracy of 0.01 g ($\approx$0.1 mN). All measurements, direct and indirect, agree with the simulated force, as shown in Fig. 2(c). The magnitude of the force shows a power-law dependence, decreasing faster near the tip of the ferritic core (note data in Fig. 2(c) is in a logarithmic scale). For distances around 20 mm and for small displacements of the order of 100 μm, force variations are small with respect to the force value ($<$1 %). Therefore, we consider constant the magnetic force exerted on the moving sphere around a fixed depth.

For the viscoelastic measurements, the coil was feed with a current pulse of $t_0 = 30$ ms and $I_0 = 30$ A. As the coil presents a finite inductance, the current pulse shows a finite rising time, that for the current setup was set to $t_r = 3$ ms, as measured experimentally, see Fig. 3. As compared with a flat (ideal) rectangular pulse, the effect of a finite rise time is to smooth the displacement waveform, i.e., the peak velocity of the embedded particle is decreased, and the peak amplitude of its oscillation is reduced. However, as long as the correct shape is introduced in the model using (5)–(7), the viscoelastic parameters can be retrieved. Also, note that if the pulse is long enough a quasi-static displacement value of $u_0 = F_0/6\pi\mu R$ will be also reached using the trapezoidal pulsed force.

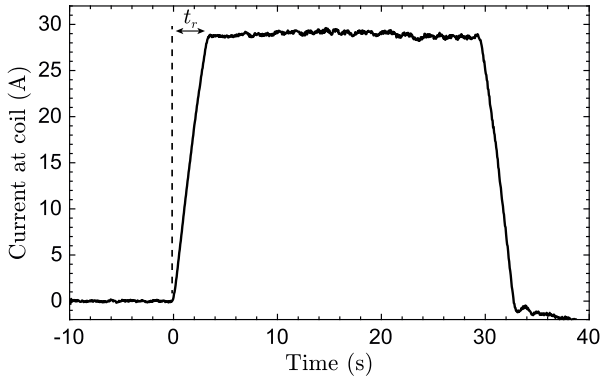

Fig. 3. Experimental electrical pulse (current) as a function of time. Dashed line marks the rising time, t_r.

B. Estimation of the Viscoelastic Parameters

For the first experiment, the displacement waveforms corresponding to phantoms A and B are shown in Fig. 4 for $I_0 = 30$ A and $t_0 = 30$ ms. The distance from the tip of the core to the sphere was estimated using ultrasound echo-impulse measurements, obtaining $z_A = 14.6$ mm for phantom A and $z_B = 15.2$ mm for phantom B. This distance was used to calculate the force acting on the sphere using (10), as given in Table I, and used for the optimization method to calculate the viscoelastic parameters. First, for the phantom A at 24.4 °C we obtain $\mu_A = 1862.6$ Pa $\pm$ 4.5 Pa, $\eta_A \approx 0.610$ Pa·s $\pm$ 0.012 Pa·s. The theoretical curve for the displacement using the retrieved parameters fits the experiments for the first 15 ms, as shown in Fig. 4(a). The ratio between the initial slope and the amplitude of the first oscillation, as well as its period is properly fitted by the viscoelastic model. When glycerin is introduced in the phantoms, as in phantom B [Fig. 4(b)], the shear modulus is increased. In addition, the first oscillation is damped proportionally to the viscous modulus. The viscoelastic model correctly fits the experimental data for this

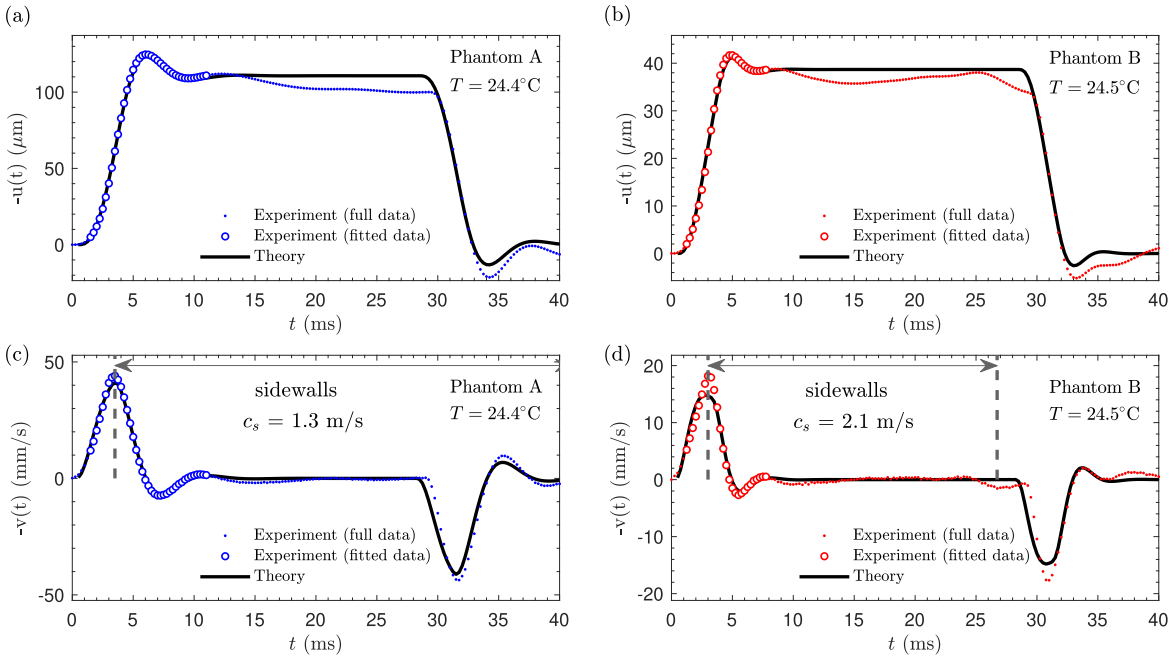

Fig. 4. Dynamics of the sphere embedded in the viscoelastic medium. (a) Displacement waveform for an individual test on the phantom A at $T = 24.4$ °C, measured experimentally (circles), using the fitted parameters and the viscoelastic theory (continuous). The data used for fitting was for $t < 8$ ms. (b) Corresponding displacement waveform for the phantom B at $T = 24.5$ °C. Velocity waveform calculated from the displacement shown in (a) from experimental displacement data (circles) and using the optimized theoretical expression in (7) for (c) phantom A and (d) phantom B.

TABLE I
ESTIMATED VISCOELASTIC PARAMETERS, AND MEASURED SPHERE LOCATION, MAGNETIC FORCE AND TEMPERATURE

	Shear elastic modulus		Shear viscous modulus	Sphere position	Magnetic force	Temperature
	Proposed method	Indentation test				
	μ (Pa)	μ (Pa)	η (Pa·s)	z (m)	F_0 (mN)	T (°C)
Phantom A	1862.6 ± 4.5	1869.6 ± 11.6	0.610 ± 0.012	14.6	3.922 ± 0.027	24.4
Phantom B	4964.4 ± 25.3	4447.4 ± 13.7	1.048 ± 0.034	15.2	3.623 ± 0.025	24.5

case too, showing, at a similar temperature, a larger shear modulus and viscous modulus than phantom A ($\mu_B = 4964.4$ Pa $\pm$ 25.3 Pa, $\eta_B = 1.048$ Pa·s $\pm$ 0.034 Pa·s). The experiment was repeated three times and the resulting viscoelastic parameters are listed in Table I. The typical error for the shear elastic modulus is of the order of 2% of the mean value while it is of the order of 10% for the viscous shear modulus. Thus, while the model of the displacement of the sphere is more sensitive to changes in the shear elastic modulus than in the viscous one, the estimation of the shear elastic parameters using the present method shows good repeatability.

It is worth noting here that theory was developed for an infinite medium. However, in practice, when the inclusion is forced to vibrate, shear waves are generated, and they propagate through the finite-size phantom. When shear waves reach the boundaries of the sample they are reflected back and, thus, the vibration of the particle is influenced by them. Fig. 4(c) and (d) illustrates the velocity signals obtained by taking the derivative of the theoretical and experimental displacement waveforms shown in Fig. 4(a) and (b). In particular, a reflection coming from the sidewalls of the container (located at a distance of $d_w \approx 25$ mm) is observed in Fig. 4(d). By considering the fitted elastic modulus, the shear wave velocity (in the low frequency limit) is $c_{s,B} \approx (\mu/\rho)^{1/2} = 2.1$ m/s. The time-of-flight corresponding to the reflection on the sidewalls is shown in gray lines in Fig. 4(d), and the reflection is visible at the sphere location, validating the calculated shear modulus. On the contrary, the low-frequency limit of the shear wave velocity for phantom A is slower ($c_{s,A} = 1.4$ m/s) and the reflection from the sidewalls arrives when the displacement pulse has already finished (at about $t = 40$ ms). Although one can argue that in this situation the plateau of the experimental displacement pulse should not manifest any deviations from the theoretical one, multiple reflections coming from other boundaries, such as the bottom ($d_b \approx 15$ mm) and top boundaries ($d_t \approx 20$ mm) of the container, prompts a noticeable distortion of the flat part of the pulse. Hence, the time window to the fit was adjusted accordingly in order to capture the dynamical response without shear wave reflections, which, for the conditions of the experiments presented in this work, results in fitting approximately the first 10 ms of the pulse, including the first oscillation. A validation was performed using the indentation tests. For both phantoms, the measured values using the penetrometer agrees the retrieved using the current method, as shown in Table I. Finally, the temperature inside the gelatin was also measured showing negligible variations between repetitions. This is extremely important in this kind of material because, as we will show in Section IV-C, shear elasticity in gelatins is strongly dependent on temperature.

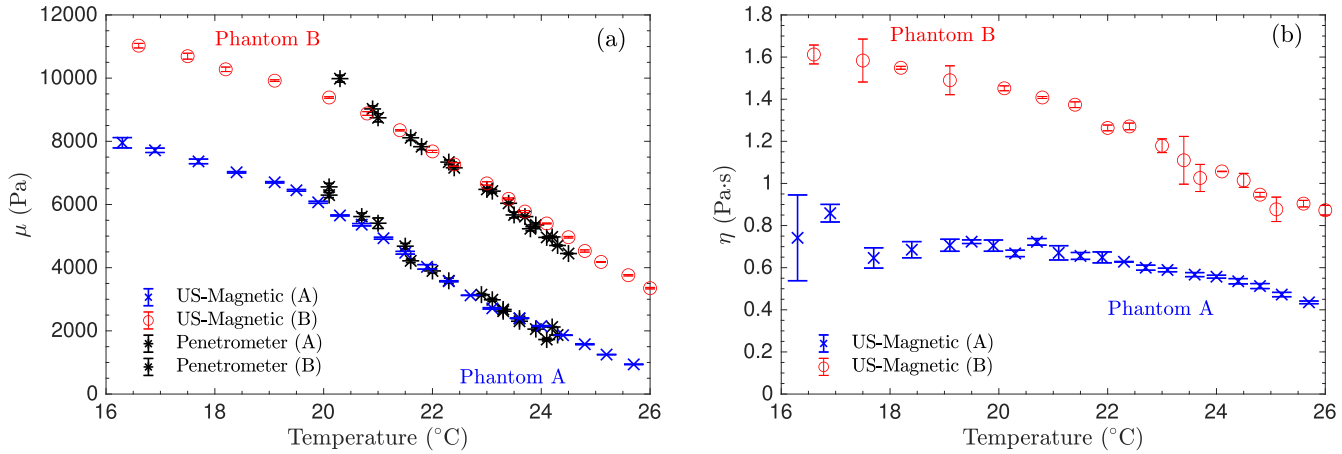

Fig. 5. Temperature-dependence of the shear elastic moduli. (a) Shear elastic modulus (μ) measured experimentally for phantom A (blue markers) and phantom B (red circles). The quasi-static elastic parameters measured using a flat-ended cylindrical indenter are shown in markers (asterisk). (b) Shear viscous modulus (η) measured experimentally at different temperatures for phantom A (blue markers) and phantom B (red circles).

C. Temperature Dependence of Viscoelastic Properties

In order to test the robustness and consistency of the viscoelastic parameters estimated using the present method, a temperature dependence study was carried out. Using the viscoelastic phantoms A and B, a set of tests were performed while temperature was slowly increased from 16° to 26 °C, i.e., up to room temperature. First, the temperature-dependent viscoelastic parameters are shown in Fig. 5(a) and (b). The estimated parameters are shown in blue (red) markers for phantom A (phantom B). On the one hand, for the real part of the shear modulus, shown in Fig. 5(a), we observe that at low temperatures the experimental data asymptotically converges to a constant value. On the other hand, the gelatin becomes softer as the temperature rises, and the shear elastic modulus decreases. Note that at a temperature around 26 °C the gelatin is about to reach a phase transition from soft-solid to viscous fluid and the method is no longer applicable.

Finally, the quasi-static viscoelastic parameters using the indentation tests are shown in Fig. 5 for both samples. The values obtained by penetrometry agree with those obtained by the proposed hybrid method for the range of measured temperatures. Both methods describe the softening of the gelatins as temperature increases and the values of elastic modulus are in good agreement.

V. Discussion and Conclusion

We propose a method to locally assess the complex shear modulus of a viscoelastic medium based on the measurement of the dynamical response of a millimeter-size soft magnetic sphere embedded on it under the action of a known magnetic force. The magnetic force was produced with a classical MMUS setup consisting of a coil and a ferritic steel core. Both, measured magnetic field and the magnetic forces acting on the sphere agree with simulations and theory. Finally, the measured displacement of the sphere inside the phantom was fitted to an incompressible Kelvin–Voigt-type viscoelastic model to obtain the shear elastic and viscous coefficients.

Two kinds of phantoms presenting different viscoelastic properties were considered: 1) water and gelatin powder and 2) water, gelatin powder, and glycerin. Their mechanical properties were monitored as a function of the temperature, showing a decrease in both the shear elastic and the shear viscous coefficients when temperature increases. The shear elastic coefficient of the different phantoms was independently validated using a quasi-static indentation technique, showing good agreement between the results of the indentation test and the proposed method combining ultrasound and magnetic forces. The maximum error was estimated to be around 10% at low temperature, although errors remain well below 5% for most temperatures.

As the generated magnetic field rapidly decays with distance, the penetration depth is limited in the present setup to 1.5 or 2 cm. Note ARF-based techniques are able to focus ultrasound beams at several centimeters. However, as most soft-solids are weak diamagnetic, the present system allows a precise estimation of the force acting on the inclusion. If the distance from the sphere to the ferritic core is measured, this system improves the reliability of the force calculation with respect to the estimated force using ARF techniques. Note the measurement of the location of the sphere can be accurately performed using the pulse-echo system. In ARF-based techniques, the force can vary due to a broad range of factors that include nonlinearities, inhomogeneities, or attenuation in the path between the transducer and the sphere. In contrast, a weak diamagnetic medium does not influence the value of the magnetic force. For this reason, the proposed technique allows a robust characterization of the medium and is able to provide not only the elastic shear coefficient but the viscous shear coefficient. Note that, as occurs with ARF-based techniques, the theory used here for the fitting assumes a homogeneous medium. If shear waves are scattered by an abrupt change of elastic properties or density, the particle vibration will be the superposition of the free oscillation and the motion due to reflected shear waves. Therefore, the method is restricted to homogeneous media. In particular, for soft-solids of shear modulus in the range 1 to 10 kPa, a volume with a radius of 15 mm around the sphere should not create strong shear wave reflections.

It is worth mentioning that MMUS imaging techniques using magnetic nanoparticles excited using an externally

applied magnetic field and then imaged using ultrasound have been proposed in the past [18]–[22]. Using its pulsed modality these techniques allow the visualization of events at molecular and cellular levels [31], [32]. The potential of this technique to assess viscoelastic properties of tissues was also pointed out but specific values were not reported [33]. Moreover, MMUS systems have been used to generate shear acoustic waves for ultrasound elastography imaging [17], [34] or to generate pulsed displacements for optical coherence elastography [35]. MMUS techniques have been applied *in vivo* [36], [37], and they have been combined with other imaging techniques such as photoacoustics [38], positron emission tomography (PET) or magnetic resonance imaging (MRI) [39]. In the proposed method, we employ a macroscopic soft magnetic inclusion instead of using magnetic nanoparticles. Because of the size of the object, the *in vivo* application of the method for tissue elastography is limited. However, due to the fact that the force and the induced displacements can be accurately described by analytical methods when using a macroscopic object, the proposed method results in a precise estimation of the viscoelastic parameters, which may have potential applications in viscoelastic material characterization in the industry. In order to envision potential applications in the medical field using this technique, replace the macroscopic object with magnetic nanoparticles will be mandatory, which will result in a more complicated estimation of the magnetic force due to the unknown distribution of the nanoparticles within the tissue. Other factors, such as a precise estimation of the magnetic susceptibility of the magnetic nanoparticles, as well as the use of larger magnetic fields and their gradients are to be taken into account. In this regard, effort has been made in the research community in order to precisely estimate the magnetic force while applying a magnetic field to magnetic nanoparticles [40], [41], making feasible to extend this technique to a more realistic preclinical/clinical application.

ACKNOWLEDGMENT

The authors would like to thank Juan Pablo Rigla for his technical support with the magnetic field characterization.

REFERENCES

[1] S. Aglyamov and A. Skovoroda, "Mechanical properties of soft biological tissues," *Biofizika*, vol. 45, no. 6, pp. 1103–1111, 2000.

[2] J. Ophir *et al.*, "Elastography: Imaging the elastic properties of soft tissues with ultrasound," *J. Med. Ultrason.*, vol. 29, no. 4, p. 155, 2002.

[3] A. Sarvazyan, "Elastic properties of soft tissues," in *Handbook of Elastic Properties of Solids, Liquids, and Gases*, vol. 3, M. Levy, H. Bass, and R. Stern, Eds. New York, NY, USA: Academic, 2001, pp. 107–127.

[4] M. T. Shaw and W. J. MacKnight, *Introduction to Polymer Viscoelasticity*. Hoboken, NJ, USA: Wiley, 2005.

[5] E. Riande, R. Diaz-Calleja, M. Prolongo, R. Masegosa, and C. Salom, *Polymer Viscoelasticity: Stress Strain Practice*. Boca Raton, FL, USA: CRC Press, 1999.

[6] L. F. Fan, L. N. Y. Wong, and G. W. Ma, "Experimental investigation and modeling of viscoelastic behavior of concrete," *Construct. Building Mater.*, vol. 48, pp. 814–821, Nov. 2013.

[7] L. Ferrari, J. Kaufmann, F. Winnefeld, and J. Plank, "Multi-method approach to study influence of superplasticizers on cement suspensions," *Cement Concrete Res.*, vol. 41, no. 10, pp. 1058–1066, Oct. 2011.

[8] S. Y. Alam and F. Hammoum, "Viscoelastic properties of asphalt concrete using micromechanical self-consistent model," *Arch. Civil Mech. Eng.*, vol. 15, no. 1, pp. 272–285, Jan. 2015.

[9] B. McKenna and J. Lyng, "Introduction to food rheology and its measurement," *Texture Food*, vol. 1, pp. 130–160, Apr. 2003.

[10] N. Jiménez, R. Picó, F. Camarena, J. Redondo, and B. Roig, "Ultrasonic evaluation of the hydration degree of the orange peel," *Postharvest Biol. Technol.*, vol. 67, pp. 130–137, May 2012.

[11] H. L. Oestreicher, "Field and impedance of an oscillating sphere in a viscoelastic medium with an application to biophysics," *J. Acoust. Soc. Amer.*, vol. 23, no. 6, pp. 707–714, 1951.

[12] Y. A. Ilinskii, G. D. Meegan, E. A. Zabolotskaya, and S. Y. Emelianov, "Gas bubble and solid sphere motion in elastic media in response to acoustic radiation force," *J. Acoust. Soc. Amer.*, vol. 117, no. 4, pp. 2338–2346, Apr. 2005.

[13] S. R. Aglyamov, A. B. Karpiouk, Y. A. Ilinskii, E. A. Zabolotskaya, and S. Y. Emelianov, "Motion of a solid sphere in a viscoelastic medium in response to applied acoustic radiation force: Theoretical analysis and experimental verification," *J. Acoust. Soc. Amer.*, vol. 122, no. 4, pp. 1927–1936, Oct. 2007.

[14] M. W. Urban, I. Z. Nenadic, S. A. Mitchell, S. Chen, and J. F. Greenleaf, "Generalized response of a sphere embedded in a viscoelastic medium excited by an ultrasonic radiation force," *J. Acoust. Soc. Amer.*, vol. 130, no. 3, pp. 1133–1141, Sep. 2011.

[15] S. Chen, M. Fatemi, and J. F. Greenleaf, "Remote measurement of material properties from radiation force induced vibration of an embedded sphere," *J. Acoust. Soc. Amer.*, vol. 112, no. 3, pp. 884–889, Sep. 2002.

[16] A. Karpiouk, S. Aglyamov, Y. Ilinskii, E. Zabolotskaya, and S. Emelianov, "Assessment of shear modulus of tissue using ultrasound radiation force acting on a spherical acoustic inhomogeneity," *IEEE Trans. Ultrason., Ferroelectr., Freq. Control*, vol. 56, no. 11, pp. 2380–2387, Nov. 2009.

[17] M. W. Urban, R. R. Kinnick, M. Mehrmohammadi, and J. F. Greenleaf, "Shear waves generated with magnetomotive force on an embedded sphere," in *Proc. IEEE Int. Ultrason. Symp.*, Sep. 2014, pp. 723–726.

[18] J. Oh, M. D. Feldman, J. Kim, C. Condit, S. Emelianov, and T. E. Milner, "Detection of magnetic nanoparticles in tissue using magneto-motive ultrasound," *Nanotechnology*, vol. 17, no. 16, p. 4183, 2006.

[19] M. Mehrmohammadi, J. Oh, S. R. Aglyamov, A. B. Karpiouk, and S. Y. Emelianov, "Pulsed magneto-acoustic imaging," in *Proc. Annu. Int. Conf. Eng. Med. Biol. Soc.*, 2009, pp. 4771–4774.

[20] T. Z. Pavan, D. R. T. Sampaio, A. A. O. Carneiro, and D. T. Covas, "Ultrasound-based transient elastography using a magnetic excitation," in *Proc. IEEE Int. Ultrason. Symp.*, Oct. 2012, pp. 1846–1849.

[21] M. Evertsson, M. Cinthio, S. Fredriksson, F. Olsson, H. W. Persson, and T. Jansson, "Frequency- and phase-sensitive magnetomotive ultrasound imaging of superparamagnetic iron oxide nanoparticles," *IEEE Trans. Ultrason., Ferroelectr., Freq. Control*, vol. 60, no. 3, pp. 481–491, Mar. 2013.

[22] A. G. Pope *et al.*, "Contrast-enhanced imaging of SPIO-labeled platelets using magnetomotive ultrasound," *Phys. Med. Biol.*, vol. 58, no. 20, p. 7277, 2013.

[23] J. F. Schenck, "Safety of strong, static magnetic fields," *J. Magn. Reson. Imag.*, vol. 12, no. 1, pp. 2–19, 2000.

[24] J. F. Schenck, "The role of magnetic susceptibility in magnetic resonance imaging: MRI magnetic compatibility of the first and second kinds," *Med. Phys.*, vol. 23, no. 6, pp. 815–850, 1996.

[25] G. E. Fish, "Soft magnetic materials," *Proc. IEEE*, vol. 78, no. 6, pp. 947–972, Jun. 1990.

[26] D. A. DeAntonio, "Soft magnetic ferritic stainless steels," *Adv. Mater. Process.*, vol. 161, no. 10, pp. 29–32, 2003.

[27] R. Fitzpatrick, *Classical Electromagnetism*. Scotts Valley, CA, USA: Createspace Independent, 2016.

[28] M. A. Lubinski, S. Y. Emelianov, and M. O'Donnell, "Speckle tracking methods for ultrasonic elasticity imaging using short-time correlation," *IEEE Trans. Ultrason., Ferroelectr., Freq. Control*, vol. 46, no. 1, pp. 82–96, Jan. 1999.

[29] J. W. Harding and I. N. Sneddon, "The elastic stresses produced by the indentation of the plane surface of a semi-infinite elastic solid by a rigid punch," *Math. Proc. Cambridge Phil. Soc.*, vol. 41, no. 1, pp. 16–26, Jun. 1945.

[30] C. T. McKee, J. A. Last, P. Russell, and C. J. Murphy, "Indentation versus tensile measurements of Young's modulus for soft biological tissues," *Tissue Eng. B, Rev.*, vol. 17, no. 3, pp. 155–164, Jun. 2011.

[31] M. Mehrmohammadi, K. Y. Yoon, M. Qu, K. P. Johnston, and S. Y. Emelianov, "Enhanced pulsed magneto-motive ultrasound imaging using superparamagnetic nanoclusters," *Nanotechnology*, vol. 22, no. 4, Jan. 2011, Art. no. 045502.

[32] M. Mehrmohammadi *et al.*, "Pulsed magneto-motive ultrasound imaging to detect intracellular accumulation of magnetic nanoparticles," *Nanotechnology*, vol. 22, no. 41, Oct. 2011, Art. no. 415105.
[33] M. Mehrmohammadi, S. Aglyamov, A. Karpiouk, J. Oh, and S. Emelianov, "Pulsed magneto-motive ultrasound to assess viscoelastic properties of soft tissues," in *Proc. 7th Int. Conf. Ultrason. Meas. Imag. Tissue Elasticity*, 2008, p. 106.
[34] T. W. J. Almeida, D. R. T. Sampaio, A. C. Bruno, T. Z. Pavan, and A. A. O. Carneiro, "Comparison between shear wave dispersion magneto motive ultrasound and transient elastography for measuring tissue-mimicking phantom viscoelasticity," *IEEE Trans. Ultrason., Ferroelectr., Freq. Control*, vol. 62, no. 12, pp. 2138–2145, Dec. 2015.
[35] V. Crecea, A. Ahmad, and S. A. Boppart, "Magnetomotive optical coherence elastography for microrheology of biological tissues," *J. Biomed. Opt.*, vol. 18, no. 12, Oct. 2013, Art. no. 121504.
[36] M. Evertsson *et al.*, "*In vivo* magnetomotive ultrasound imaging of rat lymph nodes–a pilot study," in *Proc. IEEE Int. Ultrason. Symp. (IUS)*, Oct. 2015, pp. 1–4.
[37] A. C. Bruno, D. R. T. Sampaio, T. Z. Pavan, O. Baffa, and A. A. O. Carneiro, "A hybrid transducer to evaluate stomach emptying by ultrasound and susceptometric measurements: An *in vivo* feasibility study," *IEEE Trans. Ultrason., Ferroelectr., Freq. Control*, vol. 62, no. 7, pp. 1288–1294, Jul. 2015.
[38] M. Qu *et al.*, "Combined photoacoustic and magneto-motive ultrasound imaging," in *Proc. SPIE Photons. Plus Ultrasound, Imag. Sens.*, vol. 7564, Apr. 2010, Art. no. 756433.
[39] M. Evertsson *et al.*, "Combined magnetomotive ultrasound, PET/CT, and MR imaging of 68Ga-labelled superparamagnetic iron oxide nanoparticles in rat sentinel lymph nodes *in vivo*," *Sci. Rep.*, vol. 7, no. 1, Dec. 2017, Art. no. 4824.
[40] S. R. Aglyamov *et al.*, "Elasticity imaging and sensing using targeted motion: From macro to nano," *Current Med. Imag. Rev.*, vol. 8, no. 1, pp. 3–15, Feb. 2012.
[41] I. G. Lim, S. Park, and J. Oh, "Theoretical development of a magnetic force and an induced motion in elastic media for a magneto-motive technique," *J. Korean Phys. Soc.*, vol. 69, no. 4, pp. 461–471, 2016.

Alejandro Cebrecos received the B.Sc. degree in telecommunication, sound and image, the M.Sc. degree in acoustics, and the Ph.D. degree in phononic crystals and acoustic metamaterials from the Universitat Politècnica de València (UPV), Valencia, Spain, in 2009, 2010, and 2015, respectively.

He was a Visiting Scholar with the University of Colorado at Boulder, Boulder, CO, USA, during nine months in 2014 working in numerical modeling in periodic structures and a Postdoctoral Researcher for three years with French CNRS Laboratoire d'Acoustique de l'Université du Mans, Le Mans, France, working in wave propagation in complex media, starting in 2015. He is a Postdoctoral Researcher with Instituto de Instrumentación para Imagen Molecular (I3M), Consejo Superior de Investigaciones Científicas (CSIC), UPV. He has participated in a research project for the European Space Agency, Paris, France, for noise control at launch pad using periodic structures which is now in its second stage. Nowadays, he is devoted to the development of magneto-motive ultrasound and photoacoustic imaging systems for biomedical imaging. His research is devoted to biomedical ultrasound applications as well as phononic crystals and acoustic metamaterials both in the audible and ultrasonic regimes.

Noé Jiménez (Member, IEEE) received the B.Sc. degree in telecommunication and the M.Sc. and Ph.D. degrees in acoustics from the Universitat Politècnica de València, Valencia, Spain, in 2007, 2010, and 2015, respectively.

In 2014 and 2019, he worked for the European Space Agency, Paris, France, for noise control at the launch pad using periodic structures. In 2015, he joined the French CNRS (UMR6613), Paris, for a postdoctoral position to research on deep-subwavelength acoustic metamaterials. In 2017, he enrolled Spanish National Research Council (CSIC) to research on biomedical ultrasound applications with the Instituto de Instrumentación para Imagen Molecular (I3M), Valencia. He has been a Visiting Researcher with Columbia University, New York City, NY, USA, Université du Mans, Le Mans, France, and with the University of Salford, Manchester, U.K. Since 2013, he has published more than 43 journal articles and participated in more than 150 conferences. He holds five patents. His research interests concern from fundamental research in waves in complex and structured media to biomedical ultrasound applications.

Rafael Tarazona received the B.Sc. degree in technical industrial engineering specialized on industrial electronics and M.Sc. degree in electronic systems engineering from the Polytechnic University of Valencia, Valencia, Spain, in 2002 and 2014, respectively.

He has been working as an Automation Engineer for seven years in Metallurgical Industry, Segorbe, Spain. He is currently involved in the research and technical support with Ultrasound Medical and Industrial Laboratory of the i3M, Valencia.

Miguel Company received the B.Sc. degree in industrial technologies and the M.Sc. degree in industrial engineering from the Universitat Politècnica de València (UPV), Valencia, Spain, 2015 and 2018, respectively.

He is a Researcher with the Instituto de Instrumentación para Imagen Molecular (I3M), Consejo Superior de Investigaciones Científicas (CSIC), UPV. In 2016, he enrolled the team Ultrasound Medical and Industrial Laboratory (UMIL)—I3M, Valencia, to research on magneto-motive ultrasound imaging and ultrasonic elastography techniques. His research interest concerns from developing new technologies for biomedical ultrasound applications.

José María Benlloch received the Ph.D. degree in fundamental physics from the Universidad de Valencia, Valencia, Spain, in 1991.

He was a Research Professor with Consejo Superior de Investigaciones Científicas (CSIC), Valencia. He worked with Fermi National Accelerator Laboratory, Chicago, IL, USA, and CERN, Geneva, Switzerland, on DELPHI collaboration. He also was part of the CDF collaboration that in 1995 discovered the quark top elemental particle. He worked as a Staff Member with the Massachusetts Institute of Technology, Cambridge, MA, USA, from 1991 to 1996, under the direction of Jerome Friedman. In 1996, he returned to CERN with the groups of F. Sauli y T. Ypsilantis for research on radiation detectors. In 2010, he found and he currently is the Director of the Instituto de Instrumentación para Imagen Molecular (I3M), Valencia. Since then, he has developed various diagnostic technologies based on gamma rays. He obtained ERC Advanced Grant (4D-PET) to develop new positron emission tomography (PET) technologies. He has authored or coauthored more than 300 journal articles and has supervised seven Ph.D. theses. He holds 20 patents for medical imaging. He has coordinated UE's MAMMI project on molecular imaging for early breast cancer detection, MindView FP7 project, using hybrid magnetic resonance imaging (MRI)/PET systems for brain exploration and mental disorder diagnostic, and HISTO-MRI (H2020—FET Open) on MIR systems for real-time visualization of single human cells *in vivo*.

Francisco Camarena received the Ph.D. degree in physics from the Universidad de Valencia, Valencia, Spain.

He was a Permanent Researcher with Instituto de Instrumentación para Imagen Molecular (I3M), Consejo Superior de Investigaciones Científicas (CSIC), Universitat Politècnica de València (UPV), Valencia, and a Professor with the Department of Applied Physics, UPV. He was a Founder Member and is the Head of the team Ultrasound Medical and Industrial Laboratory (UMIL), Valencia, in 2009, which forms part of the I3M, since 2016. He has authored or coauthored more than 80 national and international conferences related to acoustics and ultrasonics, and has published around 90 articles in national and international peer-reviewed journals. He has supervised 42 master's thesis and one doctoral theses.

Dr. Camarena is the head of the Chair Instituto Valenciano de Investigaciones Odontológicas (IVIO), UPV, dedicated to the promotion and development of training activities, research, dissemination, and technology transfer in the field of odontology.